Published in final edited form as:
Science. 2019 June 11; 362(6416): . doi:10.1126/science.aau1810.

In vivo modeling of human neuron dynamics and Down syndrome

Raquel Real[#1,2], **Manuel Peter**[#3], **Antonio Trabalza**[#1], **Shabana Khan**[1], **Mark A. Smith**[1], **Joana Dopp**[1], **Samuel J. Barnes**[4], **Ayiba Momoh**[3], **Alessio Strano**[3], **Emanuela Volpi**[5], **Graham Knott**[6], **Frederick J. Livesey**[3,7,*], and **Vincenzo De Paola**[1,*]

[1]Institute of Clinical Sciences, Faculty of Medicine, Imperial College London, UK, W12 0NN

[2]Graduate Program in Areas of Basic and Applied Biology, Instituto de Ciencias Biomedicas Abel Salazar, Universidade do Porto, 4050-313 Porto, Portugal

[3]Gurdon Institute and ARUK Stem Cell Research Centre, University of Cambridge, Tennis Court Rd, Cambridge, UK, CB2 1QN

[4]UK Dementia Research Institute, Division of Brain Sciences, Faculty of Medicine, Imperial College London, UK, W12 0NN

[5]University of Westminster, 115 New Cavendish Street London W1W 6UW, London

[6]EPFL, Lausanne, Switzerland, CH-1015

[7]UCL Great Ormond Street Institute of Child Health, 30 Guilford Street, London, WC1N 1EH

[#] These authors contributed equally to this work.

Abstract

Harnessing the potential of human stem cells for modelling the physiology and diseases of cortical circuitry requires monitoring cellular dynamics *in vivo*. Here, we show that human iPSC-derived cortical neurons transplanted in the adult mouse cortex consistently organized in large (up to ~100 mm^3) vascularized neuron-glia territories with complex cytoarchitecture. Longitudinal imaging of

[*]Corresponding author. vincenzo.depaola@imperial.ac.uk; r.livesey@ucl.ac.uk.

Author contributions: V.D.P. conceived and planned the live imaging, characterization and analysis of transplanted patient-derived neuron experiments, and brought F.J.L. into the project; F.J.L. independently generated the iPSC-derived neurons, conceived the *in vitro* aspects of the project and contributed to the study design. R.R., A.T. and V.D.P. performed the grafting and the two-photon imaging experiments, analyzed the data, and prepared the related figures and text; M.P. performed the human iPSC-derived neuron differentiation and *in vitro* characterization, the copy number assay, the lentiviral vector transductions and provided input on the design of the experiments; R.R. and S.K. performed cell marker immunohistochemistry, imaging and analysis for the characterization of cell identity after transplantation, and prepared the relevant figures with input from V.D.P.; R.R. conducted and analyzed the whole-brain rabies tracing reconstructions. M.A.S. performed the electrophysiology recordings in acute brain slices containing the human grafts and prepared the relevant figure and text; S.J.B. analyzed the *in vivo* calcium imaging data and prepared the relevant figures and text with input from R.R. and V.D.P.; A.M. generated and characterized the Ts21-2, WT-2 and WT-2' lines with input from F.J.L.; A. S. analyzed the gene expression, CNV and STR data and prepared the relevant figures. J.D. and S.K. characterized the graft size; J.D. characterized the axon projections from the grafts; E.V. provided input on the Hsa21 FISH experiment and analyzed the FISH data with input from V.D.P.; G.K. performed and analyzed the electron microscopy reconstructions and prepared the relevant figures. V.D.P. led the project; and V.D.P and R.R. wrote the paper with contributions from all authors.

Competing interests: None.

Data and materials availability: All data needed to evaluate the conclusion in the paper are present in the paper or the supplementary materials.

Europe PMC Funders Author Manuscripts

>4000 grafted developing human neurons revealed that neuronal arbors refined via branch-specific retraction; human synaptic networks substantially restructured over 4 months, with balanced rates of synapse formation and elimination; oscillatory population activity mirrored the patterns of fetal neural networks. Finally, we found increased synaptic stability and reduced oscillations in transplants from two individuals with Down syndrome, demonstrating the potential of *in vivo* imaging in human tissue grafts for patient-specific modelling of cortical development, physiology and pathogenesis.

Cellular analyses in the human brain are restricted mainly to post-mortem material, which cannot provide direct observation of dynamic events such as anatomical refinement (1) and the emergence of complex patterns of network activity. This limitation raises the question of how to model human neuron dynamics and their dysfunction in the many incurable disorders that affect the developing cortex (2).

Rodent models have been valuable to the understanding of the pathophysiology of complex genetic disorders such as Down syndrome (3–5), which is associated with neurodevelopmental alterations and is caused by trisomy of chromosome 21 (Ts21), but certain phenotypes are better captured in the context of a human genetic background (6). Human induced pluripotent stem cell (iPSC)-derived neurons can be used in patient-specific studies to model human cortical development (7), but *in vitro* 2D and 3D cultures (8, 9) lack key interactions with neuroglia and vasculature (10). There is an urgent need, therefore, to develop systems that more closely recapitulate the complex cellular dynamics of the living brain using patient-specific cells.

Building on previous transplantation work (11), we hypothesized that the existing physiological microenvironment in the adult mouse brain could support the expansion of human cortical tissue grafts from iPSC-derived neurons, thus allowing high-resolution, real-time *in vivo* monitoring of human neuron dynamics for extended periods of time.

Here, we used single-cell-resolution intravital microscopy (12) in human tissue grafts to gain insights into the dynamics of pruning, synaptogenesis and network activity during the earliest stages of cortical neuron development and demonstrated this approach by modelling human neuron structural and functional dynamics in Down syndrome.

Complex cytoarchitecture in human cortical tissue grafts

In order to study the dynamics of human axon and synaptic development and population activity *in vivo*, we generated cortical excitatory neurons from a control human iPSC line (13) (fig. S1) and transplanted them in the adult mouse somatosensory cortex (SCx1) for chronic multiphoton imaging (fig. 1A). Cells were transplanted after 36-38 days of differentiation, a stage at which cultures contained ~ 50% neural progenitor cells and ~ 50% deep layer cortical neurons (of which ~ 15% were T-box, Brain 1 (TBR1)+ and ~ 85% transcription factor interacting protein 2 (CTIP2)+, fig. S2A-B). As expected, and consistent with ongoing neurogenesis after engraftment, upper layer cortical excitatory neurons and a small proportion of astrocytes and oligodendrocytes could also be found both at 3 and 5 months post-transplantation (mpt) (fig. S2C-D). Electron microscopy confirmed that human

grafts resembled immature cortical tissue at 130 days post-transplantation (dpt) (fig. S3A-C), with few synapses and few myelinated axons, and showed no detectable boundary with the mouse brain (fig. S3C), suggestive of structural integration (14). Importantly, the grafts contained proliferating cells (fig. S3C-D), enlarged in size (movie S1), and consisted of multiple human- and host-derived cell types (fig. S2, S3). The cell types from the host included microglial cells, oligodendrocytes, astrocytes and both excitatory neurons and inhibitory interneurons (fig. S3, D, E and F), while no interneurons of human origin were found (n = 3 transplants). Microglia recruitment in the graft was minimal (fig. S4). Post-mortem analysis revealed that the human tissue grafts developed organizational features resembling the structural arrangement of the early fetal cortex (fig. S5)(15, 16).

At earlier stages (< 2 mpt), cortical tissue grafts contained areas with ventricular zone-like territories, with cells positive for Paired box protein 6 (PAX6), a marker of neuronal progenitors, and Nestin, a marker for radial glia, which extended processes both radially outwards from the core of the rosette-like structures (fig. S5A), and arranged in parallel (fig. S5B), mimicking the organization of radial fibers in the intermediate zone of the human fetal cortex (15). Ki67-expressing proliferating cells were found in the inner apical layer, with doublecortin (DXC)-positive immature neurons towards its basal part, extending out into the rest of the graft (16) (fig. S5A). After 2 mpt, the rosettes did not persist and, although discrete cortical laminae were not clearly visible, consistent with the fact they form in late embryonic development (around 7-month post-conception) (17), immunostaining for deep and upper layer cortical neurons with antibodies for TBR1 and Special AT-rich sequence-binding protein 2 (SATB2), respectively, showed that these cell populations can segregate *in vivo* (fig. S5C). Human astrocytes were homogenously distributed in the cortical tissue grafts (fig. S5D). Finally, human tissue grafts were vascularized as shown *in vivo* and by the endothelial marker cluster of differentiation 31 (CD31) (Fig. 1, B, C and D), suggesting that the adult mouse brain microenvironment can support the development of a multicellular transplant.

Human axon pruning imaged *in vivo*

In order to track human neurons *in vivo*, we engineered them to express GFP via lentiviral-mediated transduction prior to transplantation. Human neurons were present for the duration of our experimental time-course, which spanned up to 6 months, and spread away from the injection site (Fig. 1B, on average up to 1.2 ± 0.6 mm (mean ± SD) from bregma in the rostral direction over the first 3 mpt (n = 4 mice)). Consistent with the immature brain cell-cell interactions (10), human axons grew along blood vessels and as fiber bundles (Fig. 1E, movie S2), and parallel and radially oriented axonal layers could be detected below the dura mater (Fig. 1F; movie S3), similar to the ones found in human cortex (18).

Given the widespread axonal extension outside the graft area, we asked which brain regions human neurons target 5 mpt. Main SCx1 target areas showed a higher number of human fibers compared to areas known to receive fewer projections from SCx1 (fig. S6), suggesting the direction of axon elongation is targeted. For example, ipsilateral motor cortex, striatum, thalamus and contralateral SCx1 received more fibers than cerebellum and substantia nigra, and the corpus callosum had more axonal tracts compared to the internal capsule and

Europe PMC Funders Author Manuscripts

cerebral peduncle, (fig. S6), as expected from rodent tracing experiments (19). These data provide evidence for long-range (over centimeters) axon growth of grafted human neurons through the mouse adult brain, and indicate that while human axons are either not responsive, or can overcome, the inhibitory signals present in the adult mouse brain, they may be directed by existing guidance cues or paths.

After an initial phase of growth (20), the selective pruning of axons and dendrites is thought to normally occur via retraction and degeneration during early development (2, 21). We explored the mechanisms of human neurite pruning up to 3 mpt (Fig. 1G-L, fig. S7A-B). At this stage, neurons were still migrating (Fig. 1G) and developing neural processes in a highly dynamic mode (Fig. 1G-L). We tracked the fate of 92 human neurites from 88 cells in 6 mice at 3 mpt (fig. 1G-L). While most neurites elongated in 24h (58.4 ± 5.5%), neurite refinement was dynamic, and interchanging retraction and elongation of individual neurites over 24 h (31.0 ± 2.1%) were observed (Fig. 1I-L). Developmental neurite degeneration involves cytoskeletal destruction with widespread fragmentation over a time scale of 12-48 h (22), whereas retracting axons do not leave fluorescent fragments behind (23). Reducing the imaging interval from 24 h to 8 h showed that branch pruning (Fig. 1I) occurred mainly by retraction (91%), rather than degeneration (Fig. 1I', 9%). Axonal *en passant* boutons (EPBs), one of the two types of presynaptic specialization on cortical axons (24), could be observed in branches with a growth cone elongating (Fig. 1J). Neural processes extended long distances (maximum neurite extension = 462.769 μm in 24 h) at a speed of 10.29 ± 0.73 μm/h (fig. 1K), comparable to that observed in the neonatal mouse brain (23). Results were validated with tissue grafts from an independent control line (fig. S7A-B).

Human synaptic development imaged *in vivo*

Next, we studied the dynamics of synaptogenesis up to 4 mpt. Hallmarks of developing synaptic networks are 1) an increase in synaptic density over time, followed by pruning, and 2) the acquisition of a steady state with balanced rates of synaptic gain and loss (25). However, when and how human synaptic networks acquire these properties is unclear. We first considered dendritic spine formation and elimination (Fig. 2A-F).

After the initial phase of cell migration and neurite remodeling (fig. 1G, H), neurons stabilized allowing us to track the same cells over time (fig. 2A, fig. S8). Dendritic spines, the structural correlates of mammalian excitatory synapses (26), were seen as early as 20 dpt (32.8 ± 5.5 dpt, for either dendritic *filopodia*, considered the precursors of dendritic spines, or spines; $n = 3$ mice) (27, 28). We followed > 500 dendritic segments from 6 mice over days. However, for most dendrites, the density of synapses was too low to quantitatively study the dynamics of dendritic spines before 3 mpt, as expected from previous human fetal cerebral cortex post-mortem work (29) and the early developmental stage modeled here. Eight neurons had sufficient dendritic spine numbers at 3 mpt to calculate spine density and turnover over 3-4 consecutive sessions of 48-hour intervals (up to 6 days). The average spine density was similar to human early fetal cerebral cortex (29) and constant over the imaging period (Fig. 2C, 0.043 ± 0.006 spines/μm; $n = 70$ spines present in the first session, 176 in total; Kruskal-Wallis test, $P > 0.05$). Synaptic structures were added and eliminated at equal rates even at these early developmental stages (Fig. 2D; Wilcoxon matched-pairs signed rank

test, $P > 0.05$). The turnover ratio, a function of both spine gain and loss (30), was 46.9 ± 5.3% over 4 days (Fig. 2E), indicating synaptic reorganization.

To investigate the development of synaptic remodeling over time we repeated the same experiment after one month. Again, spine density was constant over time (Fig. 2C, 0.112 ± 0.024 spines/μm; $n = 171$ spines present in the first session, 291 in total; Kruskal-Wallis test, $P > 0.05$). However, the average spine density was increased at 4 mpt. The majority of dendrites had balanced rates of dendritic spine gain and loss (Fig. 2D, paired two-tailed *t*-test, $P > 0.05$), and only in one cell we were able to capture net synaptic pruning over 2 days (Fig. 2C, thick dashed line), consistent with the idea that a major phase of synaptic pruning occurs only at later developmental stages (28).

The turnover ratio over 4 days was 27.6 ± 3.7%, which was lower than at 3 mpt (Fig. 2E). Consistently, the survival fraction, defined as the fraction of spines surviving as a function of time, was higher at 4 mpt (Fig. 2F), suggesting stabilization of dendritic spine dynamics over time.

To more thoroughly assess synaptic dynamics, we also studied presynaptic terminals along human cortical axons (Fig. 2G-L). The density of boutons remained stable over time (Fig. 2I, 0.051 ± 0.0075 EPBs/μm; $n = 69$ EPBs in the first session, 145 in total), indicating that axonal boutons were also added and eliminated at equal rates (Fig. 2L). The turnover rate over 4 days was 45.1 ± 3.6% (Fig. 2J, K), denoting comparable dynamics between dendritic spines and axonal boutons (at 3 mpt: Mann-Whitney *U*-test, $P = 0.3394$).

In summary, we were able to study early events of human cortical neuron synaptogenesis over the first 4 mpt. Despite the low synaptic density, consistent with the primordial stage modeled here (29), there are a number of conclusions we can draw on early *in vivo* human synaptic network development. First, transplanted human neurons initially formed synaptic structures within 4-12 weeks of *in vivo* development, similar to human fetal cerebral cortex (29). Second, they underwent synaptic reorganization. Third, they progressively increased dendritic spine density over one month. Finally, human neurons balanced the rates of synaptic gain and loss over a time scale of few days.

Functional human cortical networks imaged *in vivo*

Patterned neural activity is thought to be fundamental to neural circuit development in the immature brain (31, 32). While spontaneous and sparse activity can be detected in human cortical network preparations *in vitro*, recapitulating patterns typical of early human cortical population activity, such as recurrent oscillatory bursts (32), remains challenging (33, 34).

We first investigated the electrophysiological properties of transplanted cells. We performed *ex vivo* whole-cell recordings in coronal brain slices containing the grafts (fig. S9). Current-clamp recordings were made from 18 pyramidal shaped somas ($n = 4$ mice), as identified by differential interference contrast microscopy, expression of either GFP or Td-Tomato, and by filling neurons with Lucifer yellow dye prior to post-hoc anatomical inspection (fig. S9A). Patched grafted pyramidal-like neurons were at different stages of biophysical maturation and development, with an average resting membrane potential of -53.8 ± 1.7 mV, average

capacitance of 19.4 ± 2.2 pF and average input resistance of 1.4 ± 0.1 GΩ. While cells were quiescent at resting membrane potentials, depolarizing current-steps evoked action potential firing in all pyramidal neurons tested (fig. S9B), with average action potential amplitudes of 91.3 ± 2.6 mV and half-widths of 2.2 ± 0.2 ms.

Immunohistochemistry showed glutamatergic and GABAergic terminals within the human graft (Fig. S10 A and B). To confirm that human neurons received both excitatory and inhibitory input, pyramidal shaped neurons were voltage-clamped (-70 mV) and spontaneous miniature excitatory synaptic currents (mEPSC) were observed at a frequency of 0.30 ± 0.05 Hz (5 out of 18 neurons) with an amplitude of 20.1 ± 3.2 pA, which was completely blocked by the α-amino-3-hydroxy-5-methyl-4-isoxazolepropionic acid (AMPA) receptor antagonist 2,3-dihydroxy-6-nitro-7-sulfamoyl-benzo-quinoxaline-2,3-dione (NBQX) ($n = 4$). Although synaptic events were observed in the remaining neurons, spontaneous frequency was insufficient to acquire enough events for statistical analysis (fig. S9C and S7C-D). Using a high chloride (130 mM) internal solution and in the presence of NBQX, spontaneous miniature inhibitory synaptic currents (mIPSC) were observed at a frequency of 0.24 ± 0.12 Hz (3 out of 6 neurons) with an amplitude of -73.3 ± 21.0 pA, that was fully inhibited by bicuculline ($n = 3$) (fig. S9C). Similar to mEPSC, inhibitory synaptic events were observed in the remaining neurons but insufficient events were acquired for detailed kinetic analysis. In summary, grafted neurons are excitable and fire action potentials. In addition, they receive both excitatory and inhibitory input, suggesting functional network connectivity.

To determine the origin of the afferent synaptic input to the functionally active neurons, we performed monosynaptic retrograde tracing using a modified rabies virus. This virus lacks a glycoprotein needed for replication and can only infect cells expressing the avian tumor virus receptor A (TVA) (fig. S11). Human iPSC-derived cortical progenitors and neurons were transduced with a lentiviral vector containing the TVA, nuclear GFP and glycoprotein, under the control of the human synapsin promoter (fig. S11A). Five months after the transplantation, the modified mCherry expressing-rabies virus was injected in the same location, where only grafted cells expressing the TVA are susceptible to infection. Cells that are monosynaptically connected to the infected human cells also become infected and express mCherry, allowing for accurate tracing of the neural input to the cells in the human grafts (fig. S11B). We observed that while most of the input to the transplanted human neurons comes from other human neurons (92.5% ± 1.5%, $n = 4333$ cells in 2 brains), host neurons also innervate the human graft (7.5% ± 1.5%, $n = 397$ cells in 2 brains) (fig. S11C). The traced host neurons were located within the graft, in the cortical areas adjacent to the graft, in the contralateral cortex, and in the ipsilateral CA1 hippocampal region (fig. S11B). While no traced neurons were found in other subcortical regions, thalamocortical terminals were present in the graft (fig. S10; see also fig. S12) (20). These results provide evidence that most synaptic input to the grafts comes from other human neurons. Furthermore, since no interneurons of human origin were found, these data, together with the demonstration that human neurons in the graft receive inhibitory input (fig. S9C, bottom panel), suggest that inhibition in the human grafts comes from the host.

To assess the functional development of cortical networks *in vivo*, we engineered neurons to express the genetically encoded calcium indicator GCaMP6s (35) prior to grafting and studied calcium-mediated neuronal activity *in vivo* (Fig. 3; $n = 8$ mice). Spontaneous, sparse activity (Fig. 3A-C) was detected as early as 2 weeks post-transplantation (wpt) and persisted up to 3 mpt (Fig. 3C). In addition, bursts of activity synchronized across the neuropil and multiple cells (31) were also detected at 1 mpt (Fig. 3C, inset) and persisted in all grafts tested up to 5 mpt (fig. S7E-H and movies S4, S5).

Many of these bursts had a defined spatiotemporal order (Fig. 3D,E), as well as recurrent oscillatory behavior (< 1 Hz between events; fig. 3D and S7E-I), with different incidence between 1 and 3 mpt (Fig. 3C, inset), resembling activity recorded in human developing cortex (36, 37), and consistent with a report on transplanted human cerebral organoids (38).

Recordings of calcium signals with air-puff stimulation of the animal's whiskers and facial skin, revealed that grafted neurons in the primary somatosensory cortex can be responsive to sensory stimulation (fig. S12; ~ 30% of the stimulation trials in one mouse; neither of the other two animals tested showed sensory-evoked activity), indicating that thalamocortical synapses can functionally drive activity in the human graft at 6 mpt.

Imaging human neuron structural and functional dynamics in Down syndrome

So far, we have characterized the structural and functional dynamics of human cortical neurons during the earliest phases of their development *in vivo* (fig. 1-3) and validated the main results with neurons from an independent control iPSC-line (WT-2, fig. S7). To model the *in vivo* dynamics of pruning, synaptogenesis and network activity in a complex genetic disorder, we first generated iPSC-derived progenitors and neurons from two individuals with Down syndrome (fig. S1), and then transplanted them in adult immunodeficient mice. During the reprogramming process of one of these lines (Ts21-2), we identified a disomic clone that had lost one extra copy of human chromosome 21 (Hsa21) (WT-2) (39–41). We used a microsatellite short tandem repeat (STR) assay to confirm that the parental fibroblast population was not mosaic for disomy and trisomy 21, and that Ts21-2 and WT-2 are otherwise identical to each other and the initial fibroblasts (fig. S13). This revertant disomic line (WT-2) allowed us to highlight phenotypes caused by an extra copy of Hsa21, rather than by genetic differences between individuals, without the need for multiple control lines, typically required to control for genetic variations or diverse differentiation potencies observed in genetically distinct human iPSC lines (42). Genome-wide copy number single nucleotide polymorphism (SNP) assay confirmed that the two Ts21 iPSC lines had normal karyotype, except for the extra copy of Hsa21 (fig. S14). Fluorescence In Situ Hybridization (FISH) on cortical tissue grafts further verified the presence of the extra copy of Hsa21 (fig. S15). The Ts21 lines generated progenitors, neurons and proliferating cells similarly to control grafts at 5 mpt (fig. S16 and fig. S17). Astroglia, however, were overproduced in Ts21 grafts (fig. S16), recapitulating the human pathology (43). Ts21 neurons were also present in stable locations to the end of our experimental timeline, allowing for *in vivo* single-cell-tracking (fig. S18). Chronic *in vivo* imaging revealed that Ts21 neurons had

similar rates of axon growth/retraction compared to control neurons at 3 wpt (fig. 4A-D), suggesting normal early developmental axon refinement. In addition, Ts21 neurons in the graft formed morphologically mature synaptic structures, which were plastic over time (fig. 4E-L). To determine whether dendritic spine growth was associated with synapse formation in Ts21 neurons, we reconstructed in one transplant, with electron microscopy (EM), a subset of the same dendrites after long-term *in vivo* imaging (fig. 4E, F, G). We found that newly formed dendritic spines formed synapses in 14 out of 34 cases (41%) and 6 of them (6 out of 14, 43%) within 48 hours of their first appearance. Serial EM reconstructions revealed that human dendritic spines and presynaptic terminals contained a postsynaptic density and synaptic vesicles, respectively, suggestive of complete synaptic maturation (fig. 4G). Indeed, whole-cell recordings from coronal brain slices containing the Ts21 grafts showed normal synaptic input on the DS-donor derived neurons compared to control (fig. S19, A to D), suggesting functional synaptic connections. Longitudinal *in vivo* imaging, however, showed that dendritic spines, and to a lesser extent synaptic boutons (fig. 4J-L), were more stable in neurons from both individuals with DS than in control, as demonstrated by higher survival and reduced turnover (fig. 4H, I; fig. S20). High density of GFP positive neurons prevented a quantitative analysis of synaptic dynamics in the WT-2 line. To understand whether the higher dendritic spine survival rates in Ts21 lead to higher spine density, we quantified dendritic spine density across the four lines. We found an increase in dendritic spine density in neurons from the Ts21-1 compared to WT-1 (fig. S21A), althought this increase did not reach significance consistent with post-mortem fetal DS brain analysis at ~ 5-8 gestational months (27). However, we found higher spine densities in Ts21-2 compared to WT-2, our most reliable comparison (fig. S21A). Putting the data from the two Ts21 and WT lines together highlighted a significant spine density increase in the Ts21 cells (fig. S21B). Overall, these data raise the possibility that spine density in DS cortical neurons could be higher than control, at least at the early developmental stages tested here. No difference in EPB density was found across the four lines (fig. S21 C and D).

To investigate further the increased synaptic stability phenotype, we studied neural population activity, a main regulator of postnatal synaptic refinement and stabilization (26), through *in vivo* calcium imaging of GCaMP6-expressing Ts21 grafts (fig. 4M-N). We measured both burst and global activity (see methods). These measures were reduced in Ts21 grafts (fig. 4O-Q). Together, these data highlight *in vivo* synaptic stability and functional early cortical network phenotypes in DS.

Conclusion

We investigated the earliest stages of human axon, synaptic and network activity development in a complex genetic disorder by combining live imaging in a multi-structured tissue environment and patient-specific genetic background.

Transplanted human neurons continued to develop and mature *in vivo*, in a microenvironment that retained features reminiscent of human fetal cortex, such as the large size (up to ~100 mm^3 at 5 mpt, movie S1), temporal order and duration (i.e. many months) of neurogenesis (20), vascularization, cell diversification (human-derived cortical progenitors, neurons, oligodendrocytes and astrocytes together with host-derived microglia

and vessels), as well as complex cytoarchitecture. However, the extent to which neurons in human cortical tissue grafts, either generated from human iPSCs (present study) or ESCs (20, 38, 44), can mimic the maturation, complexity and functionality of early human fetal cortical networks remains to be fully established.

Repeated imaging of single human neurons in cortical tissue grafts enabled us to gain insights on pruning, synaptic refinement, and functional neural network formation *in vivo*. We found that pruning mainly occurred by branch-specific retraction, rather than degeneration.

Nascent human excitatory synaptic networks already had balanced rates of synaptic gain and loss over ~ one week at the single cell level, suggesting that immature human neurons possess intrinsic programs of synaptic turnover regulation over relatively short time scales. Human synaptogenesis and axon growth were concurrent, rather than happening at different times, confirming previous post-mortem static analysis (28), and revealing conservation of this developmental growth program between species (45).

Oscillatory population activity had marked neuropil and soma synchronization which became more prominent over 2 months, underscoring on-going modifications of cortical circuits. Results were robust across two independent control lines, providing a basis for applying this approach, which combines live imaging in a multi-structured tissue environment with patient-specific genetic background (46), to many other neurodevelopmental diseases affecting the cortex.

Here we modeled a complex genetic disorder and saw that while developmental axon refinement was normal, synapses were more stable and neural network activity was reduced in tissue grafts from two individuals with DS, suggesting a possible role for patterned activity in regulating synaptic lifetimes in the early stages of human cortical circuit development (32). These deficits were evident even after Ts21 cells were exposed to the *in vivo* physiological microenvironment of the mouse brain for several months, indicating cell-intrinsic deficits. Consistently, using a revertant disomic iPSC line we showed that the population activity deficits were rescued by the loss of an extra copy of Hsa21, indicating that heightened expression of Hsa 21 genes is both necessary and sufficient to disrupt oscillatory burst activity in developing cortical DS networks *in vivo*.

In most previous work, human ESC or iPSCs-derived neurons have been transplanted in the damaged cortex (38, 47), spinal cord (48), striatum (49, 50) or retina (51), with the aim of cell replacement (11), rather than for disease modelling (6, 52), as demonstrated in our study. Transplantation and *in vivo* imaging for disease modelling in mice is advantageous compared to higher species such as primates, as larger numbers of animals can be used to track cells in the grafts over long periods of time, while providing a microenvironment containing vessels, immune cells and innervation, not present in common *in vitro* preparations.

In summary, we established a new *in vivo* experimental model of DS to study how the chromosomal abnormality affects the earliest stages of human axon, synaptic and functional neural network development. We expect this single-cell-resolution intravital microscopy

approach will advance the knowledge of cellular pathophysiology in this and other neurodevelopmental disorders, particularly valuable in light of the scarcity of early human fetal brain tissue material.

Supplementary Material

Refer to Web version on PubMed Central for supplementary material.

Acknowledgments

We thank Drs. Kambiz Alvian, Richard Festenstein, Tara Keck and Madeline Lancaster for comments on the manuscript. Dr. Smaragda Papadoupoulou for help with immunohistochemistry. Cher Bass and Dr. Anil A. Bharath (Imperial College London) for help with the calcium imaging analysis. Chad Whilding for developing a customized FIJI script for image analysis. Maria Tortora for help with the immunohistochemistry experiments and analysis and Carla Pernaci for help with the analysis. Maksim Lavrov and Martyna Rakowska for help with synaptic dynamics analysis. Emma Mustafa, Aleksandra Czerniak, Katie Horan, Aaron Matthews and Emma Rowley assisted with animal care and monitoring. Dr. Marco Tripodi (LMB, Cambridge) for the kind gift of the modified rabies transynaptic tracer. Prof. Gordon Stamp for the analysis of H&E stained material.

Funding: Supported by the Medical Research Council (V.D.P.); GABBA PhD program (FCT fellowship PD/BD/52198/2013), the Rosetrees Trust and ARUK (R.R.); Wellcome Senior Investigator Award (F.J.L.) and the Alborada Trust of the ARUK Stem Cell Research Centre (M.P. and F.J.L.).

References

1. Cowan WM, Fawcett JW, O'Leary DD, Stanfield BB. Regressive events in neurogenesis. Science. 1984; 225:1258–1265. [PubMed: 6474175]
2. Low LK, Cheng HJ. Axon pruning: an essential step underlying the developmental plasticity of neuronal connections. Philos Trans R Soc Lond B Biol Sci. 2006; 361:1531–1544. [PubMed: 16939973]
3. Herault Y, et al. Rodent models in Down syndrome research: impact and future opportunities. Disease models & mechanisms. 2017; 10:1165–1186. [PubMed: 28993310]
4. O'Doherty A, et al. An aneuploid mouse strain carrying human chromosome 21 with Down syndrome phenotypes. Science. 2005; 309:2033–2037. [PubMed: 16179473]
5. Gupta M, Dhanasekaran AR, Gardiner KJ. Mouse models of Down syndrome: gene content and consequences. Mamm Genome. 2016; 27:538–555. [PubMed: 27538963]
6. Espuny-Camacho I, et al. Hallmarks of Alzheimer's Disease in Stem-Cell-Derived Human Neurons Transplanted into Mouse Brain. Neuron. 2017; 93:1066–1081 e1068. [PubMed: 28238547]
7. van den Ameele J, Tiberi L, Vanderhaeghen P, Espuny-Camacho I. Thinking out of the dish: what to learn about cortical development using pluripotent stem cells. Trends Neurosci. 2014; 37:334–342. [PubMed: 24745669]
8. Shi Y, Kirwan P, Smith J, Robinson HP, Livesey FJ. Human cerebral cortex development from pluripotent stem cells to functional excitatory synapses. Nat Neurosci. 2012; 15:477–486, S471. [PubMed: 22306606]
9. Lancaster MA, et al. Cerebral organoids model human brain development and microcephaly. Nature. 2013; 501:373–379. [PubMed: 23995685]
10. Carmeliet P, Tessier-Lavigne M. Common mechanisms of nerve and blood vessel wiring. Nature. 2005; 436:193–200. [PubMed: 16015319]
11. Thompson LH, Bjorklund A. Reconstruction of brain circuitry by neural transplants generated from pluripotent stem cells. Neurobiol Dis. 2015; 79:28–40. [PubMed: 25913029]
12. Barbosa JS, et al. Neurodevelopment. Live imaging of adult neural stem cell behavior in the intact and injured zebrafish brain. Science. 2015; 348:789–793. [PubMed: 25977550]
13. Shi Y, Kirwan P, Livesey FJ. Directed differentiation of human pluripotent stem cells to cerebral cortex neurons and neural networks. Nat Protoc. 2012; 7:1836–1846. [PubMed: 22976355]

14. Emborg ME, et al. Induced pluripotent stem cell-derived neural cells survive and mature in the nonhuman primate brain. Cell reports. 2013; 3:646–650. [PubMed: 23499447]
15. Qian X, et al. Brain-Region-Specific Organoids Using Mini-bioreactors for Modeling ZIKV Exposure. Cell. 2016; 165:1238–1254. [PubMed: 27118425]
16. Hoerder-Suabedissen A, Molnar Z. Development, evolution and pathology of neocortical subplate neurons. Nat Rev Neurosci. 2015; 16:133–146. [PubMed: 25697157]
17. Saito T, et al. Neocortical layer formation of human developing brains and lissencephalies: consideration of layer-specific marker expression. Cereb Cortex. 2011; 21:588–596. [PubMed: 20624841]
18. Palomero-Gallagher N, Zilles K. Cortical layers: Cyto-, myelo-, receptor- and synaptic architecture in human cortical areas. Neuroimage. 2017
19. Zakiewicz IM, Bjaalie JG, Leergaard TB. Brain-wide map of efferent projections from rat barrel cortex. Front Neuroinform. 2014; 8:5. [PubMed: 24550819]
20. Espuny-Camacho I, et al. Pyramidal neurons derived from human pluripotent stem cells integrate efficiently into mouse brain circuits in vivo. Neuron. 2013; 77:440–456. [PubMed: 23395372]
21. Luo L, O'Leary DD. Axon retraction and degeneration in development and disease. Annu Rev Neurosci. 2005; 28:127–156. [PubMed: 16022592]
22. Nikolaev A, McLaughlin T, O'Leary DD, Tessier-Lavigne M. APP binds DR6 to trigger axon pruning and neuron death via distinct caspases. Nature. 2009; 457:981–989. [PubMed: 19225519]
23. Portera-Cailliau C, Weimer RM, De Paola V, Caroni P, Svoboda K. Diverse modes of axon elaboration in the developing neocortex. PLoS Biol. 2005; 3:e272. [PubMed: 16026180]
24. De Paola V, et al. Cell type-specific structural plasticity of axonal branches and boutons in the adult neocortex. Neuron. 2006; 49:861–875. [PubMed: 16543134]
25. De Paola V, Arber S, Caroni P. AMPA receptors regulate dynamic equilibrium of presynaptic terminals in mature hippocampal networks. Nat Neurosci. 2003; 6:491–500. [PubMed: 12692557]
26. Caroni P, Donato F, Muller D. Structural plasticity upon learning: regulation and functions. Nat Rev Neurosci. 2012; 13:478–490. [PubMed: 22714019]
27. Petit TL, LeBoutillier JC, Alfano DP, Becker LE. Synaptic development in the human fetus: a morphometric analysis of normal and Down's syndrome neocortex. Exp Neurol. 1984; 83:13–23. [PubMed: 6228436]
28. Huttenlocher PR, Dabholkar AS. Regional differences in synaptogenesis in human cerebral cortex. J Comp Neurol. 1997; 387:167–178. [PubMed: 9336221]
29. Molliver ME, Kostovic I, van der Loos H. The development of synapses in cerebral cortex of the human fetus. Brain Res. 1973; 50:403–407. [PubMed: 4705508]
30. Holtmaat A, et al. Long-term, high-resolution imaging in the mouse neocortex through a chronic cranial window. Nat Protoc. 2009; 4:1128–1144. [PubMed: 19617885]
31. Garaschuk O, Linn J, Eilers J, Konnerth A. Large-scale oscillatory calcium waves in the immature cortex. Nat Neurosci. 2000; 3:452–459. [PubMed: 10769384]
32. Khazipov R, Luhmann HJ. Early patterns of electrical activity in the developing cerebral cortex of humans and rodents. Trends Neurosci. 2006; 29:414–418. [PubMed: 16713634]
33. Kirwan P, et al. Development and function of human cerebral cortex neural networks from pluripotent stem cells in vitro. Development. 2015; 142:3178–3187. [PubMed: 26395144]
34. Quadrato G, et al. Cell diversity and network dynamics in photosensitive human brain organoids. Nature. 2017; 545:48–53. [PubMed: 28445462]
35. Chen TW, et al. Ultrasensitive fluorescent proteins for imaging neuronal activity. Nature. 2013; 499:295–300. [PubMed: 23868258]
36. Vanhatalo S, et al. DC-EEG discloses prominent, very slow activity patterns during sleep in preterm infants. Clin Neurophysiol. 2002; 113:1822–1825. [PubMed: 12417237]
37. Uhlhaas PJ, Roux F, Rodriguez E, Rotarska-Jagiela A, Singer W. Neural synchrony and the development of cortical networks. Trends Cogn Sci. 2010; 14:72–80. [PubMed: 20080054]
38. Mansour AA, et al. An in vivo model of functional and vascularized human brain organoids. Nat Biotechnol. 2018

39. Chen C, et al. Role of astroglia in Down's syndrome revealed by patient-derived human-induced pluripotent stem cells. Nature communications. 2014; 5:4430.
40. Maclean GA, et al. Altered hematopoiesis in trisomy 21 as revealed through in vitro differentiation of isogenic human pluripotent cells. Proc Natl Acad Sci U S A. 2012; 109:17567–17572. [PubMed: 23045682]
41. Weick JP, et al. Deficits in human trisomy 21 iPSCs and neurons. Proc Natl Acad Sci U S A. 2013; 110:9962–9967. [PubMed: 23716668]
42. Plona K, Kim T, Halloran K, Wynshaw-Boris A. Chromosome therapy: Potential strategies for the correction of severe chromosome aberrations. Am J Med Genet C Semin Med Genet. 2016; 172:422–430. [PubMed: 27813255]
43. Dossi E, Vasile F, Rouach N. Human astrocytes in the diseased brain. Brain research bulletin. 2018; 136:139–156. [PubMed: 28212850]
44. Mollgard K, Lundberg JJ, Beebe BK, Bjorklund A, Stenevi U. The intracerebrally cultured 'microbrain': a new tool in developmental neurobiology. Neurosci Lett. 1978; 8:295–301. [PubMed: 19605176]
45. Falkner S, et al. Transplanted embryonic neurons integrate into adult neocortical circuits. Nature. 2016; 539:248–253. [PubMed: 27783592]
46. Korecka JA, Levy S, Isacson O. In vivo modeling of neuronal function, axonal impairment and connectivity in neurodegenerative and neuropsychiatric disorders using induced pluripotent stem cells. Mol Cell Neurosci. 2016; 73:3–12. [PubMed: 26691153]
47. Tornero D, et al. Synaptic inputs from stroke-injured brain to grafted human stem cell-derived neurons activated by sensory stimuli. Brain. 2017; 140:692–706. [PubMed: 28115364]
48. Lu P, et al. Long-distance growth and connectivity of neural stem cells after severe spinal cord injury. Cell. 2012; 150:1264–1273. [PubMed: 22980985]
49. Tabar V, et al. Migration and differentiation of neural precursors derived from human embryonic stem cells in the rat brain. Nat Biotechnol. 2005; 23:601–606. [PubMed: 15852001]
50. Wernig M, et al. Neurons derived from reprogrammed fibroblasts functionally integrate into the fetal brain and improve symptoms of rats with Parkinson's disease. Proc Natl Acad Sci U S A. 2008; 105:5856–5861. [PubMed: 18391196]
51. Mandai M, et al. Autologous Induced Stem-Cell-Derived Retinal Cells for Macular Degeneration. N Engl J Med. 2017; 376:1038–1046. [PubMed: 28296613]
52. Huo HQ, et al. Modeling Down Syndrome with Patient iPSCs Reveals Cellular and Migration Deficits of GABAergic Neurons. Stem Cell Reports. 2018; 10:1251–1266. [PubMed: 29526735]
53. Israel MA, et al. Probing sporadic and familial Alzheimer's disease using induced pluripotent stem cells. Nature. 2012; 482:216–220. [PubMed: 22278060]
54. Park IH, et al. Disease-specific induced pluripotent stem cells. Cell. 2008; 134:877–886. [PubMed: 18691744]
55. Peters AJ, Chen SX, Komiyama T. Emergence of reproducible spatiotemporal activity during motor learning. Nature. 2014; 510:263–267. [PubMed: 24805237]
56. Regeur L, Pakkenberg B. Optimizing sampling designs for volume measurements of components of human brain using a stereological method. J Microsc. 1989; 155:113–121. [PubMed: 2769747]
57. Grillo FW, et al. Increased axonal bouton dynamics in the aging mouse cortex. Proc Natl Acad Sci U S A. 2013; 110:E1514–1523. [PubMed: 23542382]
58. Dubbs A, Guevara J, Yuste R. moco: Fast Motion Correction for Calcium Imaging. Front Neuroinform. 2016; 10:6. [PubMed: 26909035]
59. Barnes SJ, et al. Subnetwork-Specific Homeostatic Plasticity in Mouse Visual Cortex In Vivo. Neuron. 2015; 86:1290–1303. [PubMed: 26050045]
60. Sammons RP, Clopath C, Barnes SJ. Size-Dependent Axonal Bouton Dynamics following Visual Deprivation In Vivo. Cell reports. 2018; 22:576–584. [PubMed: 29346758]

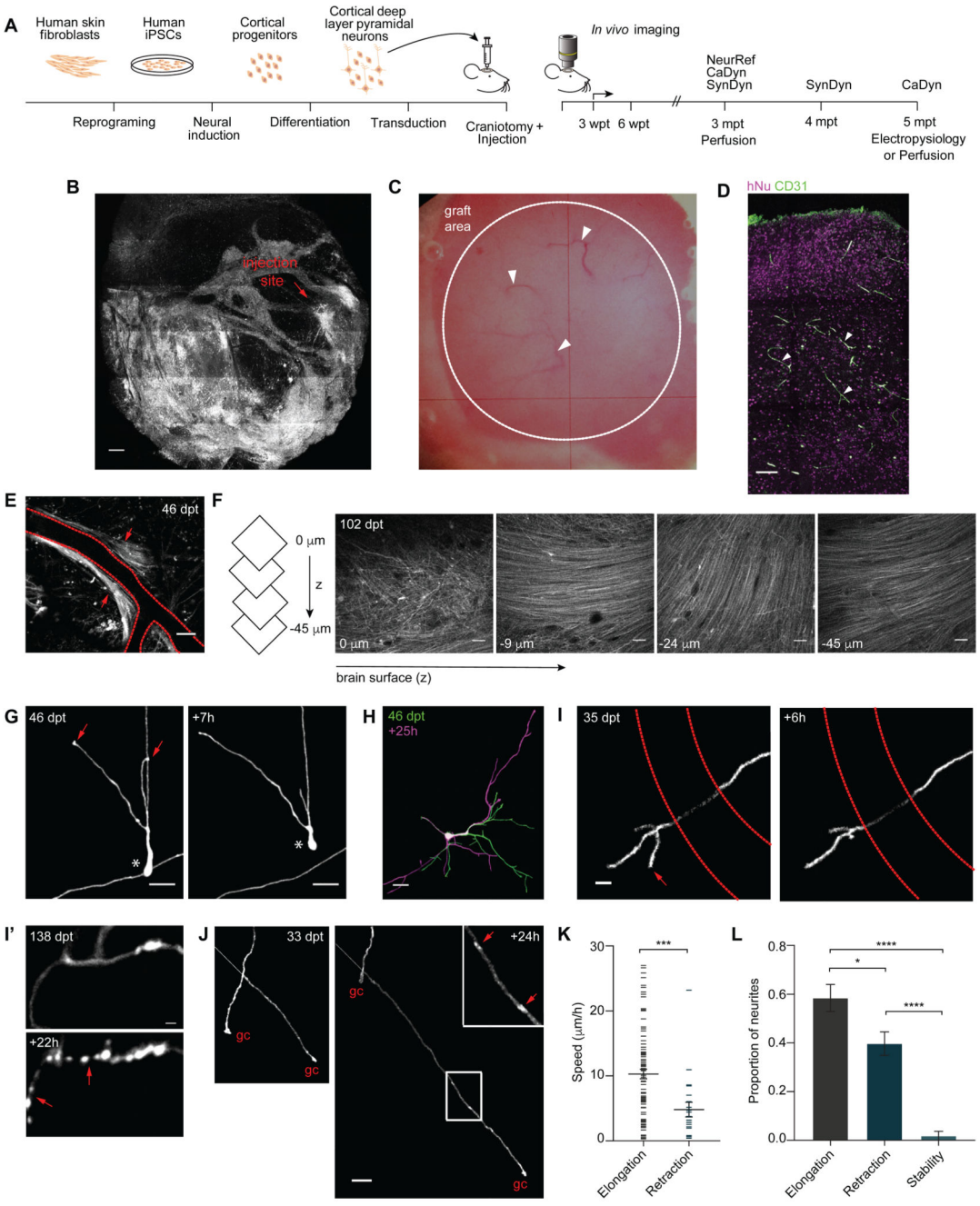

Figure 1. Single-cell-resolution *in vivo* imaging of human cortical tissue grafts reveals mechanisms of pruning.

(**A**) Schematic of experimental design (left) and 2-photon *in vivo* imaging time line (right). NeuRef, neurite refinement. CaDyn, calcium dynamics. SynDyn, synaptic dynamics. (**B**) Representative 2-photon overview of the cranial window over the injection site at 3 mpt. (**C**) Bright field view of a cranial window (~ 20 mm^2) at 5 mpt. Arrowheads indicate blood vessels. (**D**) Representative immunostaining of endothelial marker CD31 in the human graft at 5 mpt. Arrowheads indicate blood vessels. (**E**) Representative example of axonal bundles

(arrows) along blood vessels; dashed red lines represent a blood vessel. (**F**) Representative example of axonal layering in human grafts. Same example as movie S3. (**G**) Example of a human neuron migrating (*) and remodeling the leading processes (arrows) over 7h. (**H**) Representative example of extensive remodeling of a dendritic arbor in a human pyramidal neuron over 25h. (**I**) Pruning of axonal branch over 6h. Dashed red lines represent a blood vessel. (**I'**) Neurite degeneration over 22h. Arrows indicate axonal fragments. (**J**) Representative examples of axon elongation and retraction over 24h. The arrows in the inset indicate EPBs. gc, growth cone. (**K**) Speed of neurite elongation and retraction at 3 mpt (n = 113 neurites from 104 cells in 6 animals, average 17 cells/animal). Mann-Whitney U-test, ***$P < 0.001$. (**L**) Proportion of neurites elongating, retracting and stable in 24h intervals at 3 mpt (n = 92 neurites from 88 cells in 6 animals, average 15 cells/animal). Bonferroni's multiple comparisons test after one-way ANOVA, $F_{2,15} = 43.74$, $P < 0.0001$; *$P < 0.05$; ****$P < 0.0001$. Scale bars, 500 μm (B), 100 μm (D), 50 μm [(E) and (F)], 20 μm [(G), (H) and (J)], 10 μm (I), 2 μm (I').

Europe PMC Funders Author Manuscripts

Europe PMC Funders Author Manuscripts

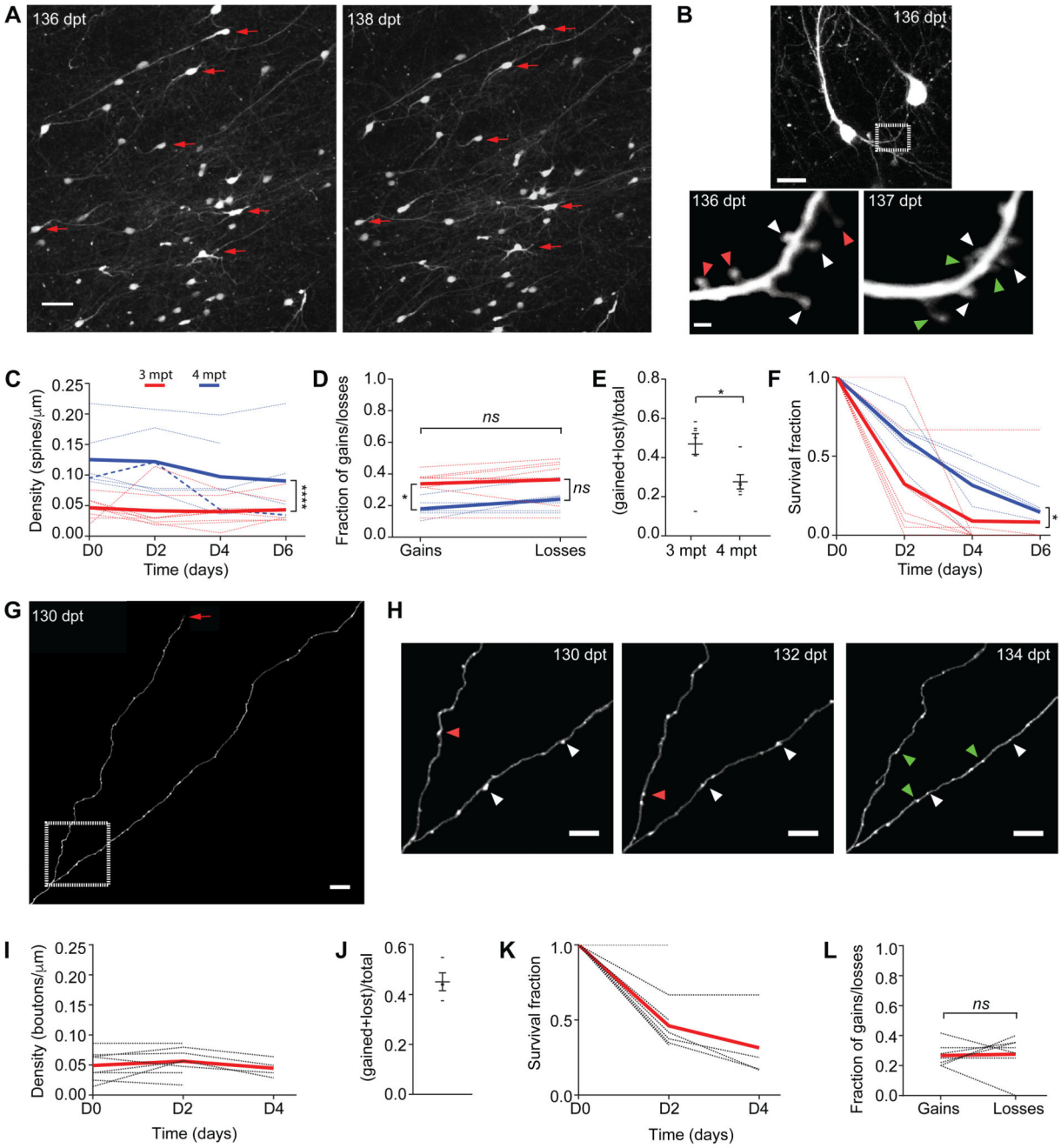

Figure 2. Developing human synaptic networks are characterized by substantial restructuring and balanced rates of gains and losses.

(**A**) Overview of cranial window at 136 and 138 dpt; red arrows represent examples of cells with a stable location over a 48h period. (**B**) Detail of a representative dendrite imaged over 24h (white box in the top panel and red box in fig. S8A); green, red and white arrowheads indicate gained, lost and stable dendritic spines, respectively. (**C**) Dendritic spine density over 4-6 days at 3 mpt (red: $n = 8$ cells, 1.40 mm total dendritic length, from 3 animals) and 4 mpt (blue: $n = 6$ cells, 0.93 mm total dendritic length, from 2 animals). Two-way ANOVA,

interaction $F_{3,46} = 0.4357$, $P = 0.7285$. ****$P < 0.0001$. (**D**) Average fraction of dendritic spines gained and lost over 48h at 3 mpt (red: $n = 8$ cells) and 4 mpt (blue: $n = 6$). Two-way ANOVA, interaction $F_{1,24} = 0.1894$, $P = 0.6673$. Sidak's multiple comparisons test, *$P < 0.05$ (gains); $P = 0.063$ (losses). (**E**) Dendritic spine turnover rate (TOR) over 4 days at 3 mpt ($n = 8$) and 4 mpt ($n = 6$ cells). Mann-Whitney *U*-test, *$P < 0.05$. Each data point represents a cell. (**F**) Dendritic spines survival fraction at 3 mpt (red: $n = 7$ cells) and 4 mpt (blue: $n = 6$ cells). Two-way ANOVA, interaction $F_{3,47} = 1.513$, $P = 0.2235$; *$P < 0.05$. (**G**) Representative example of a branched human axon at 130 dpt; arrow indicates a growth cone. (**H**) Detail of axon in (G), imaged every 48h over 4 days; green, magenta and white arrowheads indicate gained, lost and stable EPBs, respectively. (**I**) EPB density over 2-4 days at 3 mpt ($n = 8$ cells, 1.3 mm total axonal length, from 3 animals). One-way ANOVA, $F_{2,17} = 0.4014$; $P = 0.6756$. (**J**) Quantification of EPB TOR over 4 days at 3 mpt ($n = 4$ cells). Each data point represents an axon. (**K**) Quantification of EPB survival fraction at 3 mpt ($n = 8$ cells). (**L**) Average fraction of EPB gains and losses over 48h at 3 mpt ($n = 8$ cells). Wilcoxon matched-pairs signed rank *t*-test; *ns*, not significant. Dashed lines represent individual cells and full lines represent means (C, D, F, I, K, L). Scale bars, 50 μm (A), 20 μm (B, top panel), 2 μm (B, bottom panel), 10 μm (G), 5 μm (H).

Europe PMC Funders Author Manuscripts

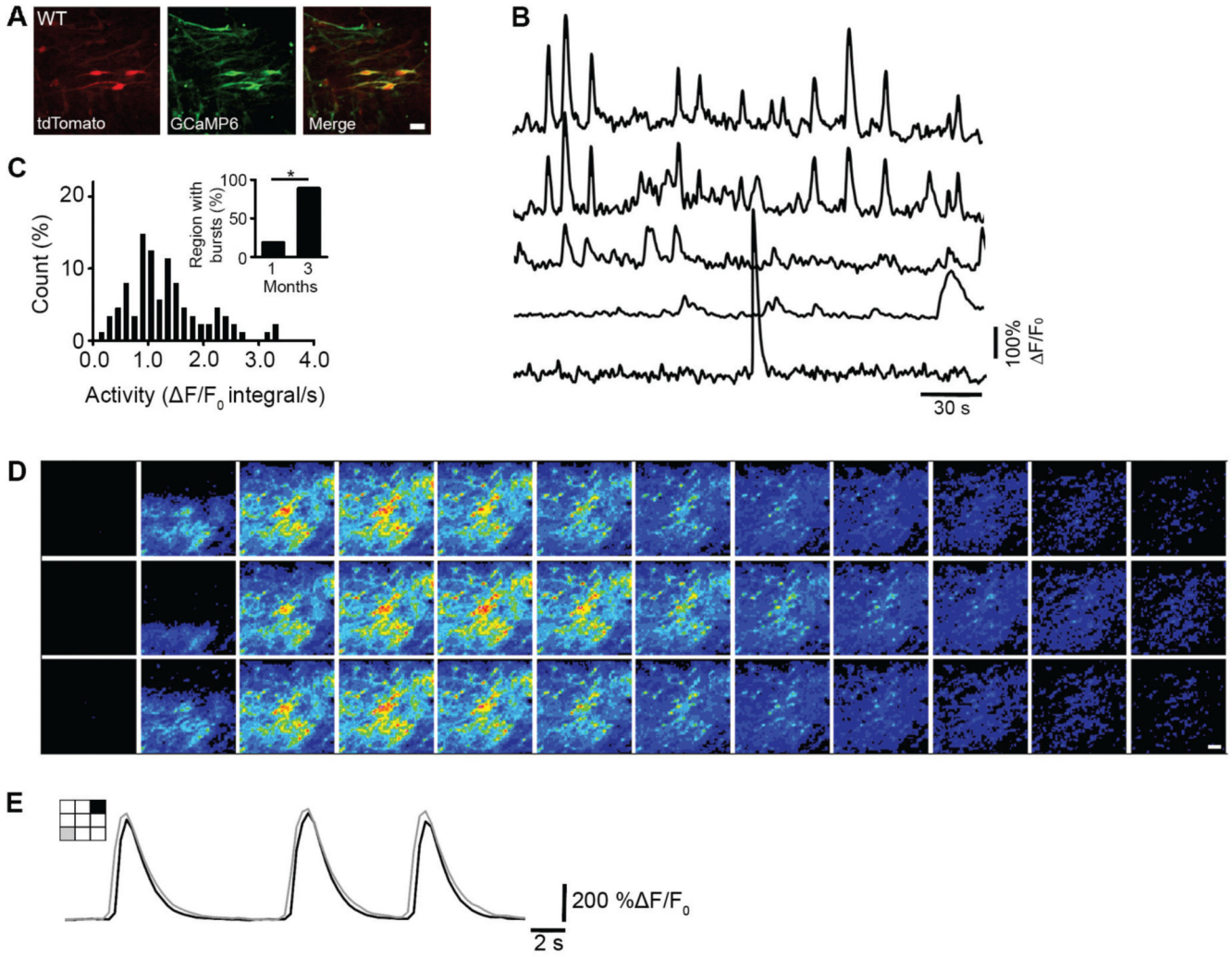

Figure 3. ***In vivo*** **calcium imaging shows that patterned population activity emerges early and has a defined spatiotemporal order.**

(**A**) Example of an imaged cortical region taken from a WT-1 graft at 1 mpt in the somatosensory cortex of an adult mouse. Neurons express tdTomato (left - red) and GCaMP6 (middle - green). GCaMP positive neurons are shown as a maximum intensity projection of activity over a 4 min period of spontaneous activity. Active neurons (yellow) are shown by overlaying the images (right – merge). (**B**) Representative $\Delta F/F_0$ calcium traces from 5 active neurons imaged in a WT-1 graft at 1 mpt. (**C**) Distribution of spontaneous calcium activity in WT-1 grafts at 1-2 mpt. Activity was measured as the integral of the average $\Delta F/F_0$ signal over the entire region of interest (ROI), normalized to the total duration of the recording in seconds ($n = 88$ cells, 6 ROIs, 3 mice). Inset: percentage of ROIs in WT-1 grafts at 1-2 mpt (3 out of 16 ROIs, 18.8%; $n = 4$ mice) and 3 mpt (31 out of 35 ROIs, 89.0%; $n = 5$ mice) that exhibit bursts. Chi-square test, $^*P < 0.05$. (**D**) Montage of image frames from a typical recurrent burst in a WT-1 graft. (**E**) Example of burst activity over two different spatial regions (gray and black) shown in left cartoon, taken from the bursts in (D). Scale bars, 10 μm (A), 20 μm (D).

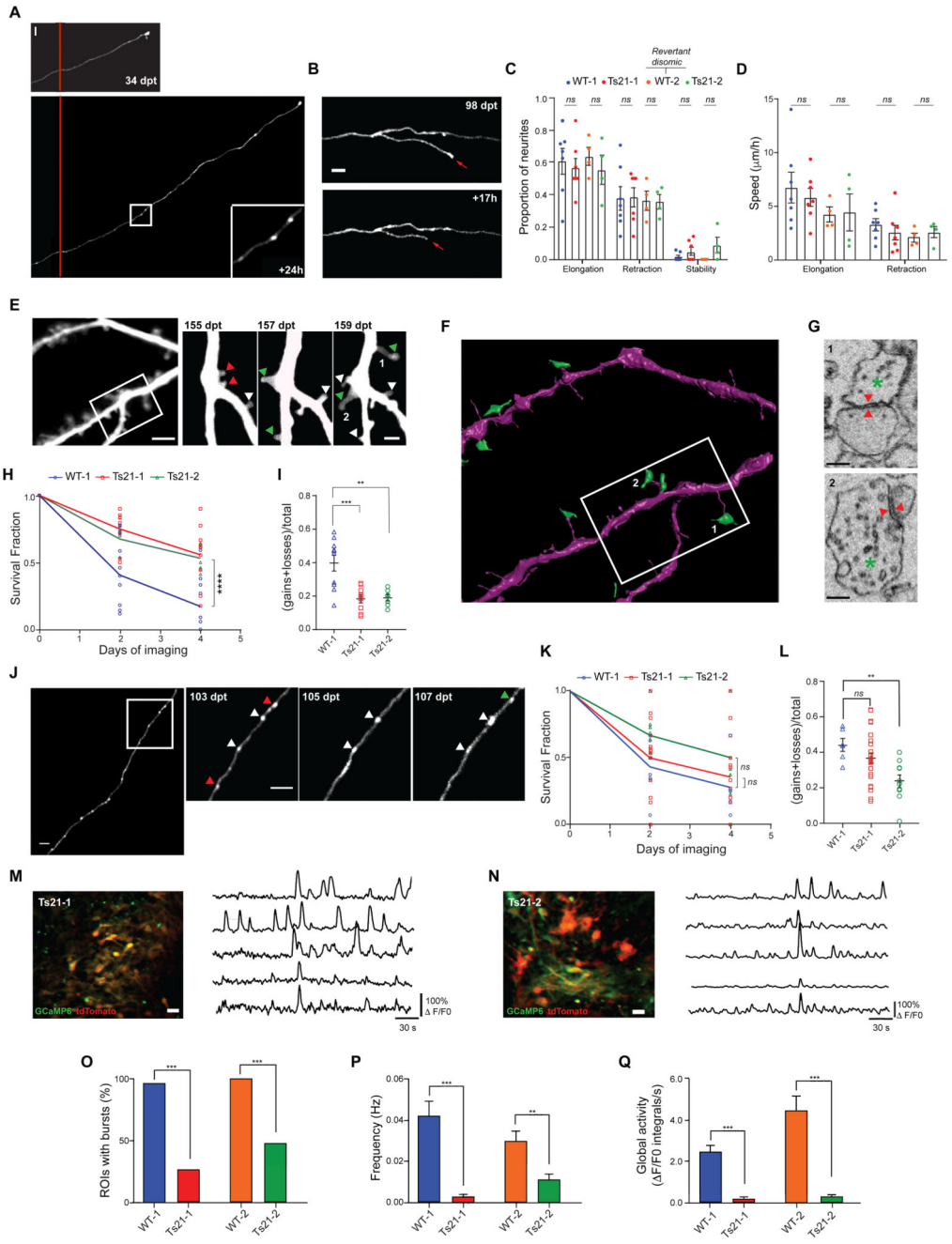

Figure 4. *In vivo* modelling of structural and functional neuronal dynamics in tissue grafts from individuals with Down syndrome.

(**A**) Representative example of axon elongation in a Ts21-1 neuron, over a 24h period. The inset highlights the presence of EPBs. (**B**) Example of axonal branch retraction in a Ts21-1 neuron over 17h. (**C**) Proportion of elongating, retracting and stable neurites in 24h intervals in WT-1 (n = 96 neurites from 79 cells, 7 grafted animals, average 11 cells/animal), Ts21-1 (n = 65 neurites from 60 cells, 7 grafted animals, average 9 cells/animal), WT-2 (n = 65 neurites from 53 cells, 4 grafted animals, average 13 cells/animal) and Ts21-2 (n = 60

neurites from 51 cells, 4 grafted animals, average 13 cells/animal) grafts at 3 wpt. WT-2 is a revertant disomic cell line from Ts21-2. Unpaired two-tailed *t*-test; *ns*, not significant. Each data point represents an animal. (**D**) Speed of neurite elongation and retraction in WT-1 (n = 96 neurites from 73 cells, average 10 cells/animal), Ts21-1 (n = 62 neurites from 54 cells, average 8 cells/animal), WT-2 (n = 53 neurites from 47 cells, average 12 cells/animal) and Ts21-2 (n = 54 neurites from 46 cells, average 12 cells/animal) grafts at 3 wpt. Unpaired multiple *t*-test; *ns*, not significant. Each data point represents an animal. (**E**) Example of dendritic branches and spines on a Ts21-1 neuron, imaged at 48h intervals for 4 days; green, red and white arrowheads indicate gained, lost and stable dendritic spines, respectively. (**F**) 3D-rendering of the same dendritic region imaged *in vivo* in (E), obtained from electron microscopy reconstruction. Presynaptic terminals are shown in green. (**G**) Electron microscopic images of the dendritic spines marked with 1 and 2 in (E). Red arrows indicate the location of synapses. Green asterisk, presynaptic terminal. (**H**) Dendritic spines survival fraction over 4 days in WT-1 (n = 10 cells from 2 animals), Ts21-1 (n = 9 cells from 4 animals) and Ts21-2 (n = 7 cells from 2 animals) grafts at 3-4 mpt. Two-way ANOVA, interaction $F_{4,69} = 5.435$, $P = 0.0007$; Tukey's multiple comparisons test, ****$P < 0.0001$. Each data point represents a cell. (**I**) Quantification of dendritic spine turnover rate over 4 days in WT-1 (n = 10 cells from 2 animals), Ts21-1 (n = 9 cells from 4 animals) and Ts21-2 (n = 7 cells from 2 animals) grafts at 3-4 mpt. Sidak's multiple comparisons test after one-way ANOVA, $F_{2,23} = 3.078$, **$P < 0.01$; ***$P < 0.001$. Each data point represents a cell. (**J**) Representative example of an axon on a Ts21-2 neuron imaged at 48h intervals for 4 days. The arrowheads in the insets indicate stable (white), new (green) and lost EPBs (red). (**K**) EPBs survival fraction over 4 days in WT-1 (n = 6 cells), TS21-1 (n = 24 cells) and TS21-2 (n = 10 cells) grafts at 3-4 mpt from 3 mice each. Two-way ANOVA, interaction $F_{4,111} = 0.8211$, $P = 0.5144$; *ns*, not significant. Each data point represents an axon. (**L**) EPBs turnover rate over 4 days in WT-1 (n = 6 cells), TS21-1 (n = 24 cells) and TS21-2 (n = 10 cells) grafts at 3-4 mpt from 3 mice each. Sidak's multiple comparison test after one-way ANOVA, $F_{2,37} = 5.588$, **$P < 0.01$; *ns*, not significant. Each data point represents an axon. (**M**), (**N**) Left: Example of imaged cortical regions taken from Ts21-1 (M) and Ts21-2 (N) grafts in the somatosensory cortex of adult mice. Neurons express tdTomato (red) and GCaMP6s (green). Active neurons (yellow) are shown by overlaying the images. Right: Representative $\Delta F/F_0$ calcium traces from 5 active neurons imaged in Ts21-1 (M) and Ts21-2 (N) grafts. Note weak synchronized burst activity across different neurons compared to the traces in fig. S7E. (**O**) Percentage of ROIs in WT-1 (50 out of 52 ROIs, 96.1 %, 6 grafted mice), Ts21-1 (10 out of 38 ROIs, 26.3 %, 3 grafted mice), WT-2 (34 out of 34 ROIs, 100 %, 3 grafted mice) or TS21-2 (11 out of 23 ROIs, 47.8 %, 3 grafted mice) grafts that exhibit bursts at 3-5 mpt. Z-test, ***$P < 0.001$. (**P**) Frequency of burst events in WT-1, Ts21-1, WT-2 and Ts21-2 grafts measured at 3-5 mpt. Kruskal-Wallis test, **$P < 0.01$; ***$P < 0.001$. (**Q**) Global ROI activity in WT-1, Ts21-1, WT-2 and Ts21-2 grafts measured at 3-5 mpt. Kruskal-Wallis test, ***$P < 0.001$. Scale bars, 10 μm [(A) and (B)], 5 μm [(E, left) and (J)], 2 μm (E, right), 0.2 μm (G), and 20 μm [(M), (N)].